



UNIVERSITAT DE LES  
ILLES BALEARS

## Master Thesis

---

# Experimental Study of the Synchronization of Two Delay-Coupled Semiconductor Lasers

---

*Author:*  
Xavier Porte Parera

*Supervisors:*  
Ingo Fischer,  
Miguel C. Soriano  
and Claudio R. Mirasso



CSIC



Instituto de Física Interdisciplinar y Sistemas Complejos



The dissertation of Xavier Porte Parera is approved:

---

Chair

Date

---

Date

---

Date

UIB, The University of the Balearic Islands

July 2011



**Experimental Study of the Synchronization of Two Delay-Coupled  
Semiconductor Lasers**

by

Xavier Porte Parera

Llicenciat en Física per la UIB (2009)

THESIS

Presented to

The University of the Balearic Islands

in Partial Fulfillment

of the Requirements

for the Degree of

MASTER OF PHYSICS

July 2011



als meus pares



# Contents

<b>Contents</b>	<b>i</b>
<b>1 Introduction</b>	<b>1</b>
1.1 Overview . . . . .	2
1.2 Semiconductor Lasers: Fundamental Properties . . . . .	2
1.2.1 Particular Features of Semiconductor Lasers . . . . .	4
1.2.2 Optical Coupling of SL . . . . .	6
1.3 Modelling the Semiconductor Laser Dynamics . . . . .	8
1.3.1 The Rate Equations Model . . . . .	8
1.3.2 The Lang-Kobayashi Model . . . . .	12
1.4 Properties of Optical Fiber-Based Setups . . . . .	14
1.4.1 Fiber Characteristics . . . . .	14
1.4.2 Advantages and Disadvantages of Fiber-Based Setups . . . . .	15
<b>2 Experimental Aspects</b>	<b>17</b>
2.1 Laser Sources . . . . .	17
2.2 Optical Fiber Elements . . . . .	19
2.3 Signal Detection . . . . .	20
<b>3 Characteristics of Semiconductor Lasers in continuous wave regime</b>	<b>23</b>
3.1 Experimental Setup . . . . .	23
3.2 Relevant Properties of Solitary Semiconductor Lasers in the Continuous Wave Regime . . . . .	24
3.3 Discussion and Summary . . . . .	31

<b>4</b>	<b>Characteristics of Semiconductor Lasers Subject to Delayed Optical Feedback</b>	<b>33</b>
4.1	Experimental Setup . . . . .	34
4.2	Effects of Delayed Optical Feedback on the Characteristics of Semiconductor Lasers . . . . .	35
4.3	Discussion and Summary . . . . .	40
<b>5</b>	<b>Synchronization of Two Delay-Coupled Semiconductor Lasers with a Passive Relay</b>	<b>43</b>
5.1	Experimental Setup . . . . .	44
5.2	Experimental Results on the Synchronization of Two Mutually Coupled Semiconductor Lasers . . . . .	45
5.3	Discussion and Summary . . . . .	56
<b>6</b>	<b>Summary and Outlook</b>	<b>59</b>
<b>A</b>	<b>List of Instruments and Components</b>	<b>63</b>
	<b>Bibliography</b>	<b>65</b>
	<b>Agraïments</b>	<b>68</b>

# Chapter 1

## Introduction

Semiconductor Lasers (SL) have changed considerably since their origins in 1962 [1]. First devices only allowed pulsed operation at liquid nitrogen temperatures. Today, SL are small and efficient devices widely used in a variety of fields. Their applications include optical data-storage, metrology, spectroscopy, material processing, pumping of other lasers and optical telecommunications.

The particular features of SL that have led to their impressive development and their application in the before mentioned fields are:

- A wall-plug efficiency greater than 60%.
- Small dimensions, typical volumes range in size from 0.1 to 1 mm<sup>3</sup>.
- Fast internal time scales that allow for high frequency modulations up to tens of GHz.
- Narrow spectral linewidth. Telecommunications SL typically exhibit optical linewidths of few tens to hundreds of Megahertz.
- Diversity of structures and properties. Modern epitaxy techniques allow individual atomic layers growth and lateral structuring, tailoring with great precision the physical properties and the device structure.
- Low costs per laser and possibility of integration in photonic integrated circuits.

A particularly interesting dynamical property of SL is their nonlinear response to external perturbations, which manifests itself in a pronounced sensitivity to effects like optical feedback or noise in the injection current. Even small amounts of re-injected light can cause the SL to exhibit chaotic emission. This effect is particularly interesting from the point of view of nonlinear dynamics (NLD). A SL subject to delayed optical feedback exhibits many characteristic high-dimensional NLD phenomena, including hyper-chaotic regimes [2] and chaos synchronization between delay-coupled

SLs [3]. Furthermore, SL are well-controlled and tunable experimental systems in which we can study very accurately various NLD phenomena.

## 1.1 Overview

In this MS Thesis, we study the nonlinear dynamical behavior of two mutually coupled SL system. We focus our investigations on the high-dimensional chaotic dynamics and the synchronization phenomena that this delay-coupled system exhibits. We optimize the experimental conditions of our setup in order to stabilize the isochronous synchronization solution.

A better understanding of the synchronization and desynchronization mechanisms of this system is also interesting from a practical point of view. It will facilitate the implementation of high speed secure communications based on chaotic carriers [4].

## 1.2 Semiconductor Lasers: Fundamental Properties

Laser operation is based on the coherent emission of light [5]. When a laser diode is pumped, charge carriers are injected into the laser. Recombination processes lead to radiative and non-radiative processes through the absorption or emission of photons in the electron-hole transitions between the conduction bands and the valence bands. The radiative processes result in the emission of photons. It is important to maximize their ratio with respect to the non-radiative processes choosing direct band-gap semiconductor materials and removing impurities. The emitted photons can be the product of stimulated or spontaneous emission. Stimulated emission is initiated by an already existing photon. Moreover, the stimulated emitted photon matches in wavelength, phase and direction of propagation with the original photon. This relation between both photons is what gives coherence to the laser emission. However, a laser only starts showing laser emission when the current exceeds a certain threshold value ( $I_{th}$ ).

Stimulated emission competes with the absorption process that creates electron-hole pairs through the absorption of already existing photons. Until the number of electrons in the conduction band doesn't exceed the number of electrons in the valence band, the stimulated emission process doesn't prevails over the absorption process. When emission equals absorption the semiconductor material becomes optically transparent. With the further increase of current, the semiconductor material exhibits optical gain and amplifies the electromagnetic radiation that passes through it. In order to achieve laser operation, an additional element is needed; an optical resonator. This resonator (cavity) provides the feedback mechanism, direction and wavelength selectivity for the stimulated emission process. The laser

cavity introduces some losses due to the transmittivity of its mirrors and to the limited confinement of light that propagates through the cavity in consecutive round trips. Furthermore, the threshold condition is defined as the pump condition where gain equals total losses (medium absorption plus cavity losses). At this injection current value for SL, stimulated emission begins to dominate and the laser emits coherently.

SL are laser sources that utilize a semiconductor material as the gain medium. In a simplified picture, a SL is a junction of p-doped and n-doped semiconductor materials. The region where these materials are in contact is called the pn-junction. When the SL is electrically pumped, in this region the electron-hole pairs recombine in photons. The semiconductor materials used for the active regions are direct band-gap materials, like GaAs or InGaP. Indirect band-gap materials, such as silicon, do not exhibit significant light emission since their transitions are phonon-mediated [6]. The side facets of the SL can act effectively as the reflecting surfaces of the optical cavity.

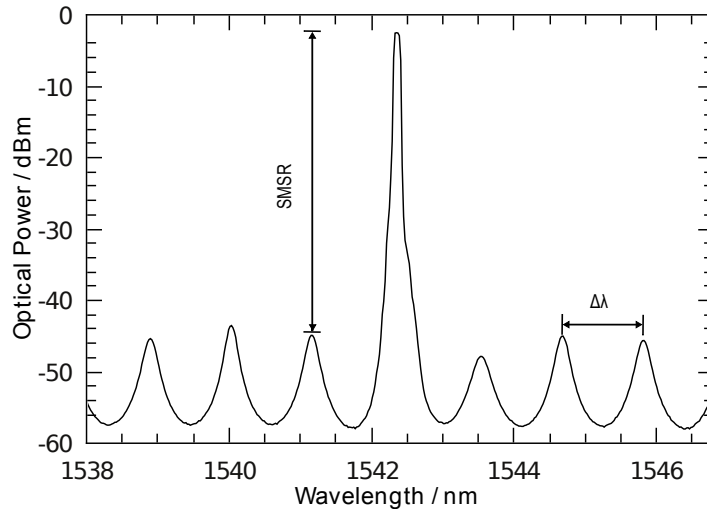


**Figure 1.1.** Experimental optical spectrum of a SL. The side modes are suppressed more than 48 dBm. The mode spacing is 1.2 nm

Figure 1.1 shows the cavity modes around the maximum gain mode for a single-mode laser near threshold (15.5 mA). The side-mode suppression ratio (SMSR) between the selected mode and the other Fabry-Perot modes is here greater than 48 dB. We can recognize the spontaneous emission level in the side-modes. The separation between different modes is here 1.2 nm and corresponds to the laser cavity resonance conditions.

There exist resonator structures different from the FP structure with interesting properties and particular applications. To illustrate different possible laser cavities we show some examples. The ring laser structure is present in many types of lasers, not only in semiconductor lasers. In a ring laser, the cavity has the shape

of a ring and light propagates through it in two possible directions: clockwise and counter-clockwise. The two counter-propagating waves in the ring cavity interfere in a pattern that changes with rotations of the laser, consequently, a widespread application for these lasers is to build gyroscopes. The distributed Bragg reflector (DBR) lasers and the distributed feedback (DFB) lasers are semiconductor lasers that have resonator cavities based on the effective reflectivities caused by interference of light when it gets reflected by the gratings. In DBR lasers two Bragg gratings are placed at both sides of the cavity acting as mirrors. In contrast, DFB lasers are lasers where the whole cavity consists of a periodic structure. This periodic structure is usually originated by modifications of the refractive index combined with a phase shift element in the middle of the cavity. Both laser structures (DBR and DFB) exhibit stable single-mode operation and are widely used in telecommunications. Finally, the vertical-cavity surface-emitting laser (VCSEL) structure has the particularity that emits light perpendicularly to the semiconductor wafer surface. The VCSELs have two epitaxially grown Bragg reflectors placed below and above the thin active medium layer. VCSELs are versatile devices. They allow for fast modulation rates, single-mode emission and easy collimation into an optical fiber, conditions that allow their use in telecommunications. Furthermore, thousands of these VCSELs are fabricated on a single wafer. Operated as laser arrays, they can achieve emission with powers in the order of watts.

### 1.2.1 Particular Features of Semiconductor Lasers

SL exhibit some particular features due to the intrinsic semiconductor medium properties. These properties have their origin in the particularities of lasing transitions in SL, which occur between two partially filled energy bands and not between discrete energy levels. The band transitions lead to a strong amplitude-phase coupling of the electromagnetic field in the laser medium variations and to the fast characteristic time scales of the SL.

The first particularity of SL is their pronounced intrinsic nonlinearity. This behavior has its origins in the strong amplitude-phase coupling of the electromagnetic field and the laser medium. This means that a small perturbation caused by spontaneous emission (inherently present in SL) or delayed optical feedback will cause a perturbation in the phase of the lasing mode.

This nonlinear effect is caused by the carrier induced variations in the real and imaginary parts of the semiconductor material susceptibility,  $\chi(n) = \chi_r(n) + i\chi_i(n)$ . The Linewidth enhancement factor ( $\alpha$  parameter) accounts for this nonlinear behavior [7]:

$$\alpha = -\frac{d(\chi_r(n))/dn}{d(\chi_i(n))/dn} \quad (1.1)$$

The linewidth enhancement factor is one of the fundamental dynamic parameters of

SL. The coupling between the electromagnetic field and the medium enhances the laser linewidth by a factor of  $1 + \alpha^2$  [7]. This parameter is particularly important for the response of the SL to a modulation and in the presence of delayed optical feedback. The modulation response of the medium will depend on frequency chirp caused by the  $\alpha$ -parameter.

The second main property of SL is their fast time scales determined by the characteristic life times of photons and carriers. The slowest time scale, which corresponds to the carrier life time, is in the sub-nanoseconds range.

In continuous-wave (CW) operation the gain and the resonator losses balance each other and the output power stays constant. External perturbations caused by spontaneous emission or spikes in the pump power lead to deviations of the output power. The power returns to the CW value through damped oscillations which are known as relaxation oscillations (RO).

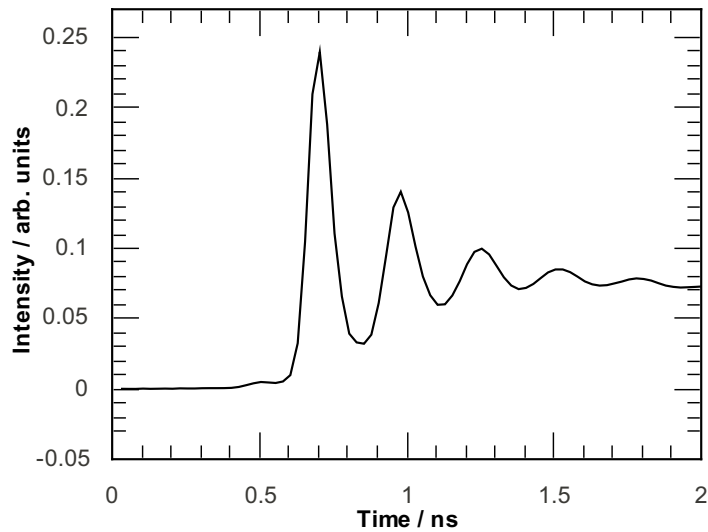


**Figure 1.2:** Experimental relaxation oscillations at the power turn on of a semiconductor laser.

Figure 1.2 depicts this typical response to a sudden power turn on. These experimental relaxation oscillations have been obtained averaging 100 times the laser response to a step function modulation. These damped oscillations represent the balancing between the carrier number and the photon number inside the cavity. Since spontaneous emission is very strong in SL [8], these RO are visible as a resonance in the SL rf-spectrum. In figure 1.3 the power spectral density versus the noise frequency is depicted. The RO resonance peak is situated at 2.6 GHz.

RO play a fundamental role in the dynamical behavior of the system. They impose an upper limit to the modulation speed of SL, typically being in the GHz range.

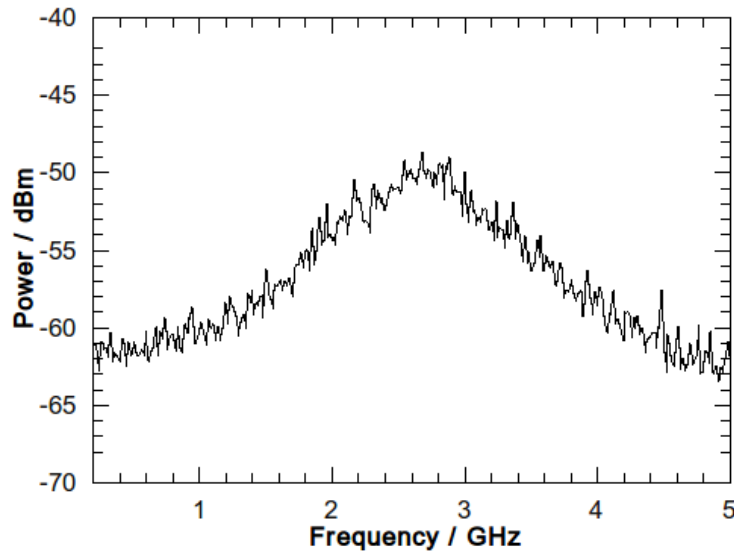


**Figure 1.3:** Experimental rf-spectrum of a SL. The RO peak is around 3 GHz.

### 1.2.2 Optical Coupling of SL

Delayed optical feedback induces instabilities in the SL emitted light. The high sensitivity to external signals has its origin in the strong amplitude-phase coupling of the electric field in the laser medium and the delay corresponding to the round trip of the light in the external cavity. Even small feedback levels give rise to a broadening of the emission linewidth from a few MHz to several GHz, a phenomenon called coherence collapse [9]. In the coherence collapse regime the dynamics can either show low frequency fluctuations (LFF) or a fully developed coherence collapse (CC) depending on the injection current and the feedback rate. Figure 1.4a shows the emitted light intensity of a SL subject to delayed optical feedback with an injection current close to the lasing threshold. The LFFs are clearly visible in this figure. These fluctuations consist in gradual increments of the emitted intensity stopped by sudden power dropouts. The characteristic frequency between power dropouts is very low in comparison with the RO frequency or the delay time. This LFF behavior has been explained as a chaotic itinerancy with a drift [10]. Figure 1.4b shows the output of the same SL at a higher injection current. The LFF behavior is lost and the emitted intensity shows what is called fully developed coherence collapse behavior. This behavior is characterized by chaotic fluctuations of the output intensity with characteristic amplitudes larger than the fluctuations in the LFF regime.

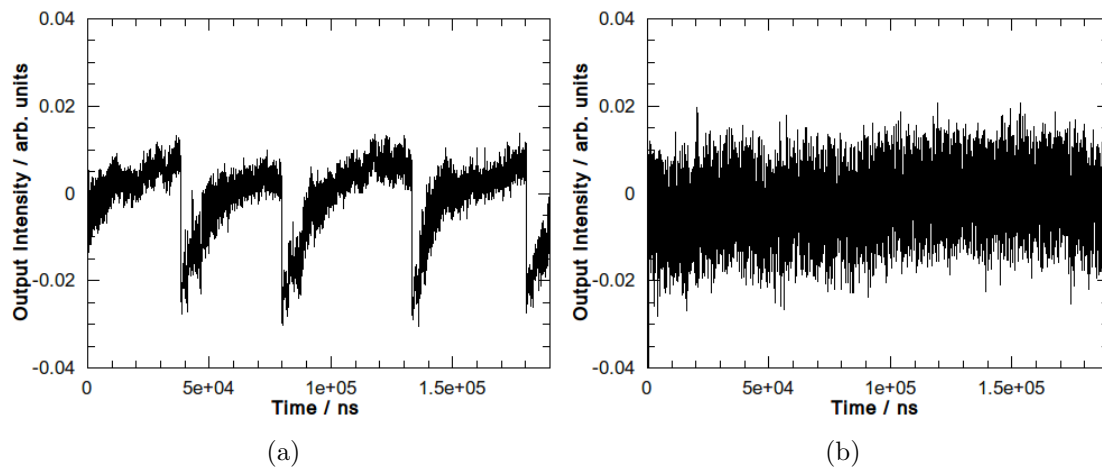


**Figure 1.4.** (a) Experimental LFF behavior of the emitted light intensity of a SL subject to delayed optical feedback. (b) Experimental CC behavior of the same SL subject to feedback at a higher injection current.

It is commonly known that coupled periodic oscillators can synchronize. This idea was first presented by Christiaan Huygens more than four centuries ago. However, this idea is not so intuitive when the oscillators are not periodic but chaotic. Nevertheless, it is well demonstrated, e. g.: two mutually coupled SL can exhibit synchronized chaotic dynamics in the sub-nanosecond time scale for weak to moderate coupling rates and long delay times [3]. Figure 1.5 shows the experimental time traces of two mutually coupled SL via their delayed optical fields in an isochronously synchronization state.

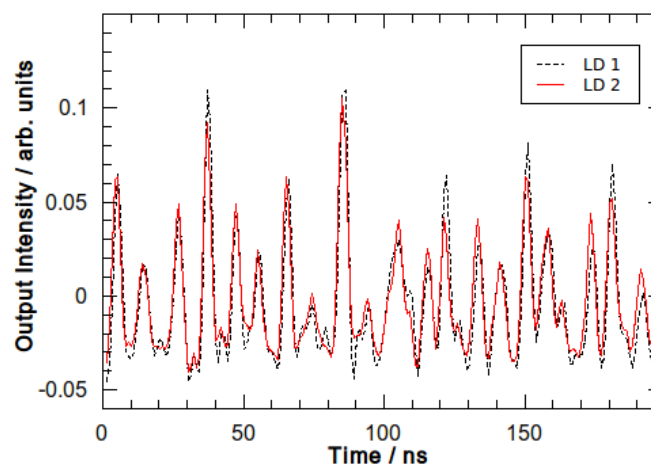


**Figure 1.5.** Experimental synchronized timetraces of two optically coupled SL with a semitransparent mirror.

Chaos synchronization can appear when both lasers have a similar emission wavelength and similar parameters. In mutually coupled schemes of two lasers, the isochronous solution is unstable [11] unless both SL have in addition a certain amount of injected light from themselves. When the isochronous solution is unstable leader-laggard type synchronization dominates, that is intensity of one SL follows the intensity of the other with a time-lag corresponding to the external cavity delay time.

## 1.3 Modelling the Semiconductor Laser Dynamics

We choose a rate equations description to model the SL dynamics with and without optical coupling. This model is a derivation based on a traveling wave model under certain conditions, limiting its validity to mono-mode SL with weak to moderate optical coupling.

The approximations used to derive this model are in reasonable agreement with our experimental conditions and its predictions are in good agreement with the dynamical behavior experimentally observed.

### 1.3.1 The Rate Equations Model

We start deriving the principal rate equations governing the behavior of the SL. This is a semiclassical model, i. e. we use a classical description for the optical field propagating in the cavity, and a quantum-mechanical description for the medium. As medium we assume a two-level medium, a rough approximation for a semiconductor medium.

We start our derivation with the picture of a SL as a simple pn-junction embedded within an optical cavity defined by its parallel external facets. When the laser is electrically pumped, we define the threshold as the situation when stimulated emission gain overcomes all losses, the cavity losses and the medium losses. Equations 1.2 and 1.3 describe the temporal dynamics of a complex electric field propagating forward and backward inside the optical cavity (see [12]), as in figure 1.6. The cavity represented is of Fabry-Perot type.

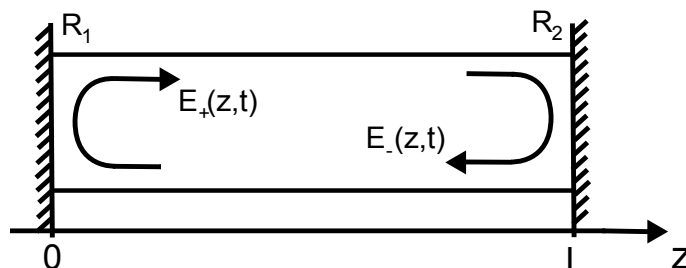


Figure 1.6: Schematic SL Fabry-Perot cavity.

$$E_+(z, t) = E_{+0}(t) \exp\left[-i \frac{n\omega}{c} z + \frac{1}{2}(g - \alpha_s)z\right] \quad (1.2)$$

$$E_-(z, t) = E_{-0}(t) \exp\left[-i \frac{n\omega}{c} (L - z) + \frac{1}{2}(g - \alpha_s)(L - z)\right] \quad (1.3)$$

$E_+$  and  $E_-$  represent the electric fields propagating in the positive and negative directions,  $n$  the refractive index of the medium,  $g$  is the optical gain due to stimulated emission and  $\alpha_s$  the optical losses inside the cavity.

A first approximation has already been done here. When an electric field propagates through a material, the medium responds to the field with a certain medium polarization. Then, our description should take into account the medium polarization dynamics. However, in semiconductors, this polarization has a very large decay rate with respect to the other two variables of the system; the electric field and the population inversion. This allows us to adiabatically eliminate the polarization and account only for two rate equations to describe the SL. This is a common approximation to classify the lasers in three different classes: A, B and C, depending on the relation between the decay rates of the electric field ( $\gamma_E$ ), the inversion ( $\gamma_N$ ) and the medium polarization ( $\gamma_P$ ) [13]. The class A lasers are characterized by large decay rates of the medium polarization  $\gamma_P$  and the inversion  $\gamma_N$ . Hence, the medium polarization and the inversion variables can be adiabatically eliminated ( $\gamma_P, \gamma_N \gg \gamma_E$ ) and the dynamics is described only by the rate equation of the electric field. In class B lasers only the medium polarization decay rate is larger than others ( $\gamma_P \gg \gamma_N, \gamma_E$ ). For class C lasers the three decay rates are of similar order of magnitude. In general, single-mode semiconductor lasers are class B lasers.

The boundary conditions at the mirror facets are  $E_{+0} = r_1 E_-(0)$  and  $E_{-0} = r_2 E_+(L)$ . From the solutions of equations 1.2 and 1.3 with these boundary conditions we can extract the lasing threshold condition and the longitudinal mode frequency at threshold ( $\omega_{th}$ ).

The gain experienced by the traveling wave after one cavity round trip (i.e.: the complex round trip gain,  $G$ ), is given by eq. 1.4.

$$G = r_1 r_2 \exp[(g - \alpha_s)L] \exp\left[-i 2 \frac{n\omega}{c} L\right] \quad (1.4)$$

↓

$$G = G_N \exp[-i(\omega - \omega_{th})\tau_{in}], \quad (1.5)$$

where  $\tau_{in} = \frac{2n_g L}{c}$  is the internal round trip time,  $n_g = n + \omega \frac{\partial n}{\partial \omega}$  is the group refractive index and  $G_N$  is the non-frequency dependent term of the round trip gain, given in equation 1.3.1.

$$G_N = \exp\left[(g(N) - \alpha_s)L + \ln(r_1 r_2) - 2i \frac{\omega_{th} L}{c} \frac{\delta n}{\delta N} \Big|_{th} (N - N_{th})\right]$$

After one complete cavity round trip, the magnitude of the electric field will be increased in a factor described by the following expression:

$$E(t + \tau_{in}) = GE(t). \quad (1.6)$$

For operating conditions close to threshold, we can make the assumption that the complex electric field oscillates at  $\omega \sim \omega_{th}$ . We linearize the dependence of the gain and the frequency on the carrier number. This linearization is described in equations 1.7 and 1.8:

$$g(N) \simeq g_{th} + \xi(N - N_{th}) = g_{th} + \xi\Delta N \quad (1.7)$$

$$\omega(N) \simeq \omega_{th} + \omega_N(N - N_{th}) = \omega_{th} + \frac{\alpha}{2}\xi\Delta N \quad (1.8)$$

$\xi$  represents the differential gain ( $\xi \propto \frac{\delta g}{\delta N}|_{th}$ ), and  $\alpha$  stands for the linewidth enhancement factor.

This approximation has two main consequences. First, as  $(\omega - \omega_{th})$  is small, the electric field after one round trip can be approximated by  $E(t + \tau_{in}) \simeq G_N E(t)$ . Second, since  $\omega_{th}$  is much faster than the typical variation of the envelope of the electrical field  $E(t)$ , we can apply what is called the slowly-varying envelope approximation (SVEA). We suppose that the variation of the optical field in time can be described in units of the internal round trip time,  $\tau_{in}$ :

$$\frac{dE(t)}{dt} \simeq \frac{E(t + \tau_{in}) - E(t)}{\tau_{in}} \Rightarrow \frac{dE(t)}{dt} \simeq \frac{G_N - 1}{\tau_{in}} E(t) \quad (1.9)$$

In edge emitting SL typical cavity dimensions are in the range of  $300 - 500 \mu m$ , which results in  $\tau_{in} \approx 10 ps$ . This time is the same order of magnitude than the photon lifetime ( $\tau_E \sim 1 ps$ ) and smaller than the carrier lifetime ( $\tau_N \sim 1 ns$ ).

Using the linearizations of eqs. 1.7 and 1.8, and including the linearization of the expression of  $G_N$  we can deduce the first rate equation corresponding to the complex electric field. The second rate equation, describing the carrier number, is derived from the evaluation of the density matrix for an ensemble of two-level atoms. The carrier number is related with the occupation of states in valence and conduction bands. The assumption that the semiconductor media is a two energy levels medium is only possible due to the big difference between the intra-band relaxation time and the carrier lifetime in the semiconductor material.

The carrier equation accounts for the constant addition of carriers via DC pumping, and for the losses due to spontaneous and stimulated emission.

The resulting rate equations (expressed as in [14]) are the following:

$$\frac{dE(t)}{dt} = \frac{1}{2}(1 + i\alpha)\xi n(t)E(t) \quad (1.10)$$

$$\frac{dn(t)}{dt} = J - \gamma_N n(t) - (\Gamma + \xi n(t))|E(t)|^2 \quad (1.11)$$

$n(t) = N(t) - N_{th}$ ,  $J$  is the pump current above the threshold, normalized to the electron charge,  $\Gamma$  accounts for the total loss rate of photons and  $\gamma_N$  is the carrier decay rate.

These two equations allow for damped periodic solutions for the intensity  $|E|^2$ , corresponding to the previously explained Relaxation Oscillations (RO). These periodic solutions can emerge from oscillations of energy among the carrier reservoir and the photon reservoir [8]. The corresponding frequency is defined as:

$$\omega_{RO} = \sqrt{\frac{v_g \xi N_p}{\tau_p}}, \quad (1.12)$$

where  $\xi$  is the differential gain,  $v_g$  is the group velocity in the gain medium,  $N_p$  is the averaged photon density and  $\tau_p$  is the photon lifetime in the cavity.

### 1.3.2 The Lang-Kobayashi Model

The rate equations describe the SL dynamics in CW operation. We tackle the problem of a SL subject to moderate rates of delayed optical feedback. The Lang-Kobayashi (LK) model extends the equations 1.10 and 1.11 for the solitary laser including an additional feedback term to the field equation in order to describe the dynamics of a SL subject to delayed optical feedback. For the complete derivation of this model see [15]. The equations read [16]:

$$\frac{dE(t)}{dt} = \frac{1}{2}(1 + i\alpha)\xi n(t)E(t) + \gamma E(t - \tau)e^{-i\omega_0\tau} \quad (1.13)$$

$$\frac{dn(t)}{dt} = J - \gamma_N n(t) - (\Gamma + \xi n(t))|E(t)|^2 \quad (1.14)$$

where  $\gamma$  represents the coupling strength,  $\tau$  is the external cavity delay time and  $\omega_0$  is the optical frequency. The feedback term  $\gamma E(t - \tau)e^{-i\omega_0\tau}$  takes the amount of feedback and the phase difference after one external cavity round trip into account. In fact, this phase difference is highly sensitive to any mechanical changes of the cavity length due to the large typical values of the optical frequency. So minimal distortions in the delay length change significantly this delay phase. The feedback rate ( $\gamma$ ) quantifies the amount of optical feedback and  $\tau$  is the external cavity delay time.

The fixed points of the LK equations can be found making an Ansatz of the form of a plane wave for the electric field amplitude with constant optical frequency ( $\omega_0 + \Delta\omega$ ) and a constant value for carrier number ( $n$ ). Each of the fixed points is given by solving the following equations:

$$\Delta\omega\tau = \gamma\tau\sqrt{1 + \alpha^2} \sin\{(\omega_0 + \Delta\omega)\tau + \arctan \alpha\} \quad (1.15)$$

$$(\gamma\tau)^2 = \left(\Delta\omega\tau - \alpha\frac{\tau\xi n}{2}\right)^2 + \left(\frac{\tau\xi n}{2}\right)^2 \quad (1.16)$$

The solutions of the transcendental equation 1.15 are the intersections between a line and a sinusoidal function and are located on an ellipse in the  $(\Delta\omega, n)$ -space. These solutions are typically called external cavity modes (ECM) and are always created (and annihilated) in pairs of stable (*Modes*) and unstable (*Antimodes*) fixed points [17]. Physically they correspond to constructive (Modes) and destructive (Antimodes) interference conditions of the coupled cavities. The excentricity of the ellipse is determined by the  $\alpha$  parameter. The bigger the value of  $\alpha$ , the more elongated is the shape of the ellipse. The SL dynamics evolves in time in the phase space with the ECM. The trajectory of the SL dynamics in the  $(\Delta\omega, n)$ -space (see [9] and [10]) evolves chaotically from the destabilized low gain mode, close to the solitary laser mode, to higher gain modes. But, at a certain point, when the trajectory is

approaching the maximum gain mode, a fatal encounter with the stable manifold of an antimode (saddle point) can occur and the trajectory is ejected back to some point near the solitary laser mode. At this point, the chaotic cycle starts again.

### *Chaos Synchronization of Two Delay-Coupled SL*

The previously explained Lang-Kobayashi model can be extended to two mutually coupled semiconductor lasers with self-feedback. Each SL has a delayed feedback contribution from itself and another from the respective other laser as in figure 1.7. The system is described by the following set of four coupled differential equations:

$$\begin{aligned}\frac{dE_{1,2}(t)}{dt} &= \frac{1}{2}(1 + i\alpha)\xi n_{1,2}(t)E_{1,2}(t) + \gamma(E_{1,2}(t - \tau) + E_{2,1}(t - \tau))e^{-i\omega_0\tau} \quad (1.17) \\ \frac{dn_{1,2}(t)}{dt} &= J - \gamma_N n_{1,2}(t) - (\Gamma + \xi n_{1,2}(t))|E_{1,2}(t)|^2 \quad (1.18)\end{aligned}$$

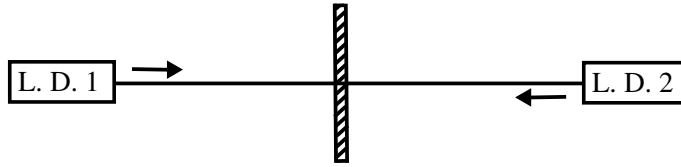


**Figure 1.7.** Schematic picture of two SL optically coupled with a semitransparent mirror acting as passive relay.

Equations 1.17 and 1.18 correspond to the complex electric field and carrier number for the two semiconductor lasers. The coupling coefficients, the delay times and the optical frequencies are equal for both SL. The dynamical regimes of this coupled system depend on two main system parameters: the input current and the feedback/coupling strength.

Chaotic dynamics and synchronization do not exclude each other. The occurrence of sensitive dependence on initial conditions and stable synchronization can relate to different directions in the phase space (see [18]). The direction where the chaoticity develops then corresponds to the synchronization manifold. We associate this development with positive parallel Lyapunov exponents. In the transversal direction we can have either negative or positive transversal exponents. The negative transversal exponents give rise to stable synchronization. The positive ones give rise to unstable synchronization.

In delay-coupled SL we can only have transversal stability of the solutions if each one of the SL has a certain amount of light coming from a relay in between the two lasers. In our system (fig. 1.7) this relay consists of fiber optics equivalent to a semitransparent mirror. This is called a passive relay. An active relay could consist in a third SL just between the other two [19].

## 1.4 Properties of Optical Fiber-Based Setups

SL subject to delayed optical feedback and/or coupling have so far mostly been studied in free-space optics. This section will explain the reasons as to why we have used fiber-optic setups. In this section we introduce the most important properties of optical fibers, making them useful for our coupled laser experiments.

### 1.4.1 Fiber Characteristics

An optical fiber is an optical waveguide based on the principle of total internal reflection. In its simplest form it consists of a central core surrounded by a cladding whose refractive index is slightly lower than that of the core. Finally, some annular external jacket is usually used to strengthen the fiber. Figure 1.8 shows a schematic view of an optical fiber. The material used in actual low-loss optical fibers is low cost silica glass  $SiO_2$ . The increment of the core refractive index is caused by the use of dopants for the core. Dopants like  $GeO_2$  or  $P_2O_5$  are usually employed. The confinement of the light within the fiber depends on the fiber geometry and composition. A very important property of an optical fiber is the number of internal modes it supports. The de-dimensionalized frequency  $V$  (usually called V-number) determines the number of modes supported by the fiber:

$$V = k_0 a \sqrt{n_1^2 - n_2^2}, \quad (1.19)$$

where  $n_1$  and  $n_2$  are the indexes of the core and cladding respectively,  $k_0 = 2\pi/\lambda$ ,  $a$  is the core radius and  $\lambda$  is the wavelength of light.

It can be demonstrated [20] that the condition for a fiber to support only one mode is  $V \leq 2.405$ . We usually work in the wavelength range of  $\lambda \sim 1550nm$ . The radius of a single-mode fiber core at this wavelength is  $a \simeq 5\mu m$ .

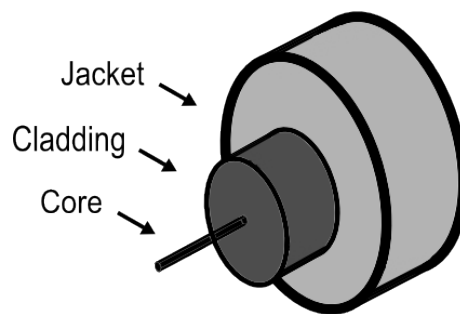


**Figure 1.8:** Schematic view of an optical fiber.

The structure depicted in figure 1.8 is called step-index structure. Actually there exist more complicated structures for optical fibers depending on the properties desired for the fiber. For example, Graded-index fibers reduce drastically the modal

dispersion when light propagates through the fiber. Polarization maintaining (PM) fibers avoid the polarization mode dispersion problems inherent to symmetric optical fibers. Finally, photonic-crystal fibers are microstructured fibers with arrays of holes inside. These holes can be placed with different geometries and filled with different gases changing the intrinsic waveguiding properties of the fiber.

Optical fibers play an important role in the field of telecommunications. The two main problems present in light transmission through a fiber are attenuation and dispersion. The improvement in the fabrication processes have reduced the attenuation from the typical values in the 60s of  $\sim 1000\text{dB}/\text{km}$  to  $\sim 0.2\text{dB}/\text{km}$  in the  $1550\text{nm}$  domain nowadays. Dispersion problems have been partly solved with improvements in fiber structures and manufacturing.

Under our laboratory conditions, none of the previous characteristics represent a problem for the experimental work. One challenge optical fibers introduce for our purposes are the difficulties to control light polarization. Any change in temperature or stress along the fiber will cause birefringence and a consecutive local change in the polarization of light inside the fiber.

## 1.4.2 Advantages and Disadvantages of Fiber-Based Setups

Fiber-based setups have many advantages and some disadvantages with respect to free-space setups. Traditionally, most of the research on delay-coupled SL have been done in free-space setups. The following points are a comparison between both setups:

### *Mechanical Stability:*

Free-space setups often imply stability problems that come from the difficulties to mechanically stabilize the optical pathway containing different elements. An edge-emitting SL is a very small device with an astigmatic output that is hard to collimate properly. Any temperature change or vibration can result in de-collimation of the beam and cause a loss of stability of the whole cavity. Fiber-based setups do not have such mechanical stability problems when the SL is already fiber-coupled, and the device is fiber-pigtailed.

### *Polarization of the Light:*

This is an issue in fiber-based setups. In free-space setups the polarization of the whole experiment can be well determined with one polarizer along the light path. In fiber-based setups the birefringence of the optical fibers can cause significant modifications in the polarization state of the light. The fiber paths are vulnerable to temperature changes and bending.

***Cavity and Coupling Lengths:***

Free-space and fiber-based cavities and coupling paths have typical lengths that differ in one order of magnitude. Common fiber components have typical lengths in the order of meters. When used in a coupling setup the coupling lengths also result to be in the order of meters. In contrast, free-space setups can be implemented with coupling lengths in the order of few meters down to centimeters. Different cavity lengths allow exploring different dynamical regimes. We can distinguish between short-cavity and long-cavity regimes comparing the external cavity round trip time with the RO characteristic time. If they are of the same order of magnitude we refer to the short-cavity regime, while if the delay times are much larger than the RO period we refer to the long-cavity regime. Fiber-based setups are naturally in the long or even very long-cavity regimes.

***Scalability:***

Scalability is one of the main advantages of fiber-based setups. In free-space optics the difficulty to make the setup stable grows with the number of optical elements. Setups involving more than three delay-coupled lasers are almost impossible to stabilize. In fiber-based setups this difficulty is almost inexistent. You can split and couple light into various branches as long as your power is sufficient. Particular attention needs to be paid to control of spurious back reflections.

# Chapter 2

## Experimental Aspects

In the preceding chapter, we have already introduced the main elements employed in our experiments, the semiconductor lasers and the optical fibers. This chapter gives more insight into these elements and complementing components, explaining our experimental setup in detail. We motivate why we choose certain components, by linking them to the role they play in the experiment.

In the first section, we introduce the laser sources and explain the particular features exhibited by these SLs. In the second section, we explain the optical fiber components. Finally, in the third section, we focus on the detection devices and the different measurements we can perform with them.

First of all, before introducing the individual elements in our setup, the laboratory environment deserves attention. Our laboratory has been shielded against external electromagnetic waves by a surrounding Faraday cage, in order to shield the experiment from wireless and radio frequencies which are in the same frequency range than the SL typical RO dynamics (GHz range). These external fields could cause undesired modulations and perturbations in the recorded measurements.

### 2.1 Laser Sources

The main interest of the present work relies in the exploration of synchronization of two mutually-coupled semiconductor lasers. Synchronization can only be obtained if both SLs are similar, typically matching in parameters by few percent. One way to achieve almost identical properties and internal dimensions is to choose them from the same semiconductor wafer.

The SL used for our synchronization experiments have been hand-selected to match. The chosen lasers exhibit single-mode emission and narrow linewidth. The lasers have been manufactured by *Eblana Photonics*<sup>1</sup>. The type of lasers we use is called Discrete Mode Laser Diode (DMLD) [21]. They have a particular device structure

---

<sup>1</sup>Specific reference to components and instruments is listed in appendix A

based on a Fabry-Perot (FP) cavity with a small number of etched structures along the laser cavity. These etched structures change the refractive index in the cavity manipulating the FP cavity loss spectrum, resulting in a suppression of all cavity modes except one. Another characteristic of the laser packages is the absence of optical isolators at the laser output. Commercial telecommunications SL packages typically have such an optical isolator at the output to avoid back reflections that could destabilize the CW emission. Obviously, since we will use these particular devices for optical coupling purposes, optical isolators are not desired.

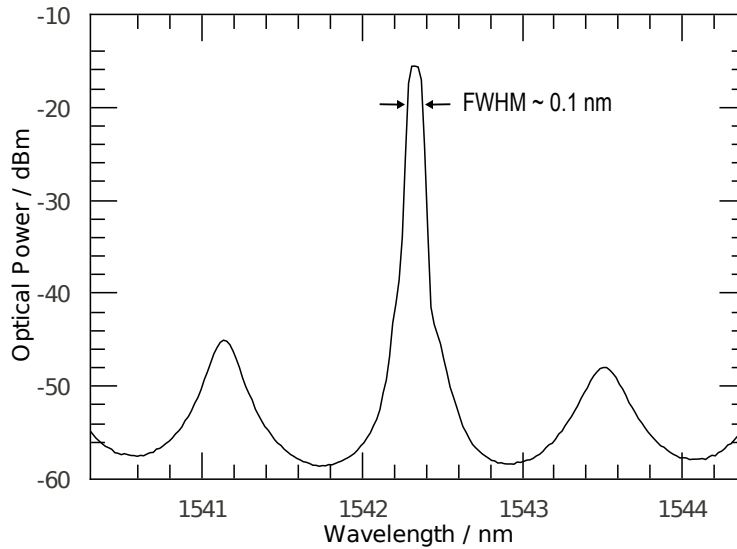


**Figure 2.1:** Experimental optical spectrum of a DMLD.

Figure 2.1 depicts an experimental spectrum of a DMLD at 15 mA ( $I_{th} = 11.85$  mA). At this injection current and temperature (22 °C) the emission wavelength measured by a grating spectrometer is 1542.3 nm with a full width half-maximum (FWHM) of 0.1 nm, the resolution limit of the optical spectrum analyzer. The side-modes are suppressed by 28 dB with respect to the main mode, which has almost 290 times more power than the side-modes. In chapter 3, we will give further details on the dependence of the emission wavelength on injection current and temperature, the dependence of the RO peak on the injection current and the measurement of the linewidth enhancement factor.

Our DMLD are butterfly packaged and mounted via modules that have an integrated temperature controller (TEC) with a peltier element and a thermistor to set and control the laser working temperature. The butterfly module is pigtailed with a single-mode fiber (SMF) with angled end connector (FC/APC). The laser current and temperature are controlled (Thorlabs PRO8000) with an accuracy of  $\pm 0.01$  mA and  $\pm 0.01$  °C.

## 2.2 Optical Fiber Elements

All experimental setups employed here are fiber-based. In the previous chapter, we discussed the advantages and disadvantages of fiber-based setups versus free-space setups. This section aims to provide information of the fiber-based devices we use in our experiments.

Our setup is composed of SMF components, specified for 1550 nm with a tolerance of  $\pm 40$  nm. This wavelength corresponds to optical communication wavelengths, the so called third window. It is the mostly used wavelength range for long-range telecommunications, because it is the one that implies lowest losses. The fibers have FC/APC connectors, i. e. the input and output ends of the fiber are cleaved at an  $8^\circ$  angle, which minimizes undesired back reflections from fiber connections.

Particular fiber components we use in the experiments are fiber couplers and fiber isolators. Our fiber couplers have two input fibers and two output fibers like the one depicted in figure 2.2:

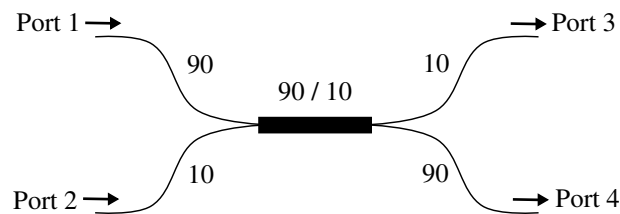


**Figure 2.2:** Schematic picture of a fiber coupler.

Light from one input exits at both opposite outputs with a proportion that depends on the coupling percentage. The fiber coupler depicted in fig. 2.2 is a 90/10 coupler. The light from of the inputs is split in a proportion of 90 to 10 at the opposite two outputs. Note that the couplers do not have a predefined directionality.

Fiber couplers can be fabricated fusing both fiber cores at the contact point. This causes a coupling of the mode from the mode that is propagating into the fiber to the other fibers in contact.

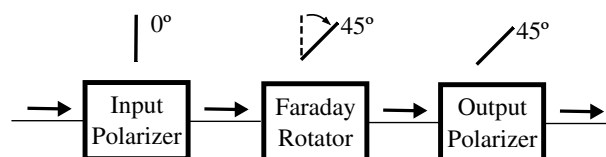


**Figure 2.3:** Schematic picture of the internal parts of a fiber optical isolator.

Figure 2.3 depicts the schematic structure of a fiber-based optical isolator. We can see that fiber isolators are composed by two polarizers and one Faraday rotator. Light injected in the forward direction is linearly polarized, shifted  $45^\circ$  after the Faraday rotator and passes through the second polarizer without loss. The light propagating in the reverse direction is isolated due to the  $90^\circ$  shift respect to the input polarizer.

In chapter 1 we explained that one particularity of fiber-based setups is the difficulty to control the polarization of the light. The polarization inside the fibers is changed by the birefringence, which is induced by stress and temperature changes. For this reason we use fiber polarization controllers in our setup. Fiber polarization controllers (Thorlabs FPC560) are designed to perform controlled polarization changes. They utilize stress induced birefringence to change the polarization state of the light. Figure 2.4 shows an schematic view of a FPC. The number of loops in the three paddles are 1, 2 and 1 respectively. This configuration allows for modifying the polarization to any state. The  $\lambda/2$  plate can either change the orientation of linearly polarized light or exchange the handedness of circularly polarized light. The  $\lambda/4$  plate interchanges linearly to circularly polarized light and vice versa. To be able to change from any polarization state of light to any other we need to align the fast axis of the fiber properly by adjusting the paddles manually.

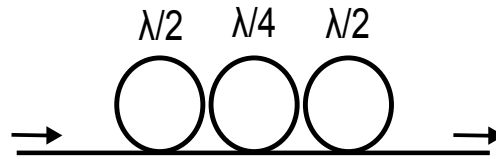


**Figure 2.4:** Schematic picture of a fiber polarization controller (FPC) with three paddles.

## 2.3 Signal Detection

Semiconductor lasers subject to delayed optical feedback exhibit dynamics on different time scales. For instance, low frequency fluctuations have typical frequencies in the MHz range while the RO frequencies are in the order of GHz. The same wide range of frequencies can be found in the optical spectra. The external cavity modes are typically separated by hundreds of MHz and the laser diode modes are separated by hundreds of GHz. The detection setup has to account for these multiple temporal and spectral scales. Each one of the following devices measures different quantities and covers different ranges:

- The optical power meter (Thorlabs PM30) is used to measure the optical power the SL emits. It is composed by a slow p-i-n-photodiode with sensitivity in the 700-1800 nm window and a power resolution @ 1550 nm of  $\sim 1$  nW.

- The optical spectrum analyzer (Anritsu MS9710C) is a grating spectrometer that measures the optical spectrum of the SL with enough precision (0.1 nm) to resolve the longitudinal modes of the diode cavity, which are separated in our lasers by  $\simeq 1.2$  nm. The detection bandwidth of the optical spectrum analyzer (OSA) ranges from 600 to 1750 nm.
- Fast photodiodes (Miteq DR-125G-A) with 13 GHz bandwidth detect the intensity dynamics of the system. The output signal from the photodiodes is electrically amplified before arriving to the oscilloscope or to the electrical spectrum analyzer.
- The electrical spectrum analyzer (Anritsu MS2667C) measures the frequency and amplitude of the signal coming from the photodiode in the frequency domain. The detection bandwidth of the electrical spectrum analyzer (ESA) ranges from 9 kHz to 30 GHz. A DC block at the input of the ESA blocks frequencies  $\leq 7$  kHz.
- A high bandwidth oscilloscope (LeCroy SDA816Zi) detects the output signal from the photodiode in the time domain. The oscilloscope bandwidth is 16 GHz and we can measure simultaneously 4 channels at a sampling rate of 40 GS/s.



# Chapter 3

## Characteristics of Semiconductor Lasers in continuous wave regime

This chapter explores the relevant properties of a solitary SL in the CW regime. In the first section of this chapter we introduce the experimental setup. In the rest of the chapter, we present experimental results concerning the properties of a solitary semiconductor laser and, finally, we discuss these results in the third section.

The characterization of the solitary laser is needed to determine the fundamental parameters of the laser diode. The dynamical behavior of the laser will depend on these parameters. In particular, these results determine the influence of delayed optical feedback in the laser behavior. The knowledge of the properties of the solitary lasers are important to know when synchronization in the bidirectional coupling scheme can be achieved. Two SL will only synchronize if they are sufficiently similar, with a maximum parameter mismatch of a few percent.

### 3.1 Experimental Setup

Figure 3.1 depicts the schematic of the setup we have used for the characterization of the dynamical properties of the solitary SL in the CW regime.

The laser is a fiber-pigtailed discrete-mode laser diode (DMLD) driven by a low noise constant current source. Temperature and current are stabilized with an accuracy of about 0.01 °K and 0.01 mA, respectively. An optical isolator is placed before the detection line in order to shield the laser from undesired back reflections. We need an external optical isolator since our DMLD modules do not have a built-in optical isolator as explained in chapter 2. The time-averaged output power can be measured when a power-meter is attached directly after the optical isolator.

In order to detect different magnitudes besides the time-averaged output power, the setup includes a 90/10 fiber coupler attached to the optical isolator. Ten per cent is used for the optical spectrum analyzer (OSA) and ninety for the fast photodiode (13 GHz bandwidth).

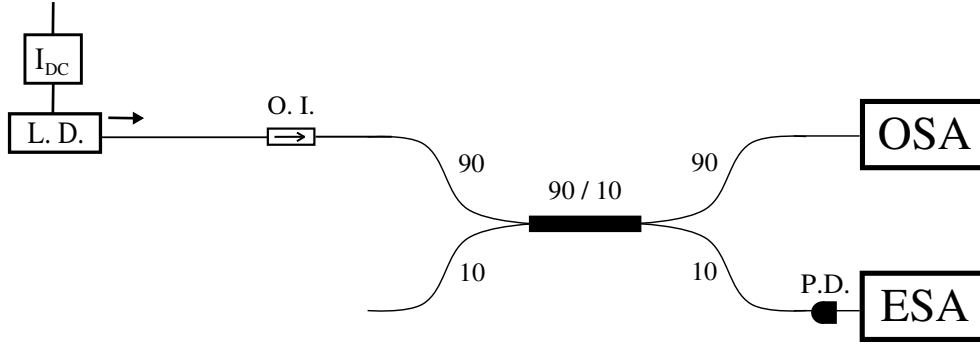


**Figure 3.1.** Experimental setup of one laser diode (LD) driven with a constant current source ( $I_{DC}$ ). An optical isolator (OI) is attached to the LD. The optical isolator output is attached to a 90/10 coupler and its outputs to the optical spectrum analyzer (OSA) or to a fast photodiode (PD) connected to the electrical spectrum analyzer (ESA).

The optical spectrum is detected by the OSA, while the power spectrum of the intensity fluctuations is measured by the fast photodiode and the ESA.

## 3.2 Relevant Properties of Solitary Semiconductor Lasers in the Continuous Wave Regime

Experimental data is recorded directly from instruments using LabView software. A custom-made program manages the interaction with the instruments via GPIB or USB buses. The LabView interface allows for scanning different parameters, e. g.: the injection current or temperature. The corresponding data is then acquired for each parameter setting.

### *Power-Current Characteristics*

One of the most important characteristics of a SL to be measured is the relation between the current injected in the device and the light it emits. This relation is called the output power vs. input current curve, or PI curve. A PI curve can be divided into two distinct regions with different slopes. As the injected current is increased the laser emission is first dominated by spontaneous emission. In this region the output power increases quadratically with the number of carriers [8]. The point where the slope of the PI curve changes drastically is referred to as the threshold current,  $I_{th}$ . This value denotes the current where stimulated emission starts to dominate. The threshold current is a first measure of the SL efficiency. The lower  $I_{th}$ , the easier it is to achieve laser operation.

Figure 3.2 depicts the PI curve of one of our SL (Eblana DMLD) at 22 °C. First points demonstrate spontaneous emission increasing quadratically with the injection current (explicitly depicted at the inset). The threshold point separates the sponta-

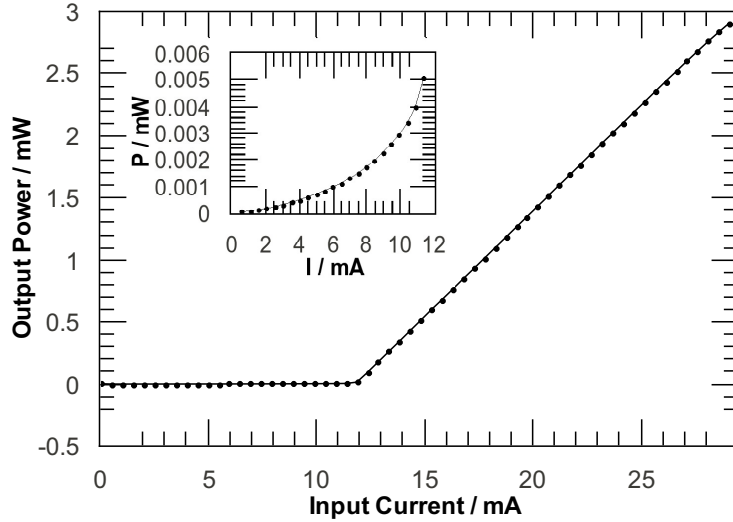


**Figure 3.2.** Characteristic PI curve of a DMLD at 22 °C. The inset magnifies the behavior under threshold.

neous emission dominated behavior from the laser operation regime, dominated by stimulated emission. This threshold current can be found as the cross point between the linear fit of the points above threshold and the x-axis. In our case the threshold current is  $I_{th} \simeq 11.81$  mA. We can observe that the points above the threshold current follow a linear increase. This linearity of the laser operation reflects the linear dependence of the photon density in the laser cavity with the current above threshold. In the range of currents shown in figure 3.2 the laser emission presents no power saturation.

The slope of the PI curve above threshold is directly related to the efficiency of the laser device. This slope has units of mW/mA and tells us how many mW of power the laser outputs for every 1 mA increase in its injection current. The parameter related to the slope of the PI curve is the external differential quantum efficiency  $\eta_d$  [22]. In real lasers not all the recombinations of electron-hole pairs lead to photons contributing to the laser emission. Some recombinations are non-radiative and other recombinations can result in spontaneous emission. These effects reduce the efficiency of the laser from the theoretical quantum limit given by the relation  $(hc)/(\lambda q)$ . Where  $h$  is the Planck's constant ( $h = 6.6262 \cdot 10^{-34} J \cdot s$ ),  $q$  is the electron charge ( $q = 1.6022 \cdot 10^{-19} C$ ),  $c$  is the speed of light ( $c = 2.99 \cdot 10^8 m/s$ ) and  $\lambda$  is the photon wavelength ( $\lambda = 1.542 \cdot 10^{-6} m$ ).

For the calculation of  $\eta_d$ , the slope of the PI curve is divided by  $(hc)/(\lambda q)$ . We have accounted for the emission of only one facet. In our laser  $\eta_d = 21\%$ . This small value of efficiency is probably the result of a long cavity with high values of internal losses and due to the coupling efficiency between the laser and the fiber pigtail.

Temperature variations change the slope of the PI curve and the threshold value. For higher temperatures the laser becomes less efficient and the threshold current

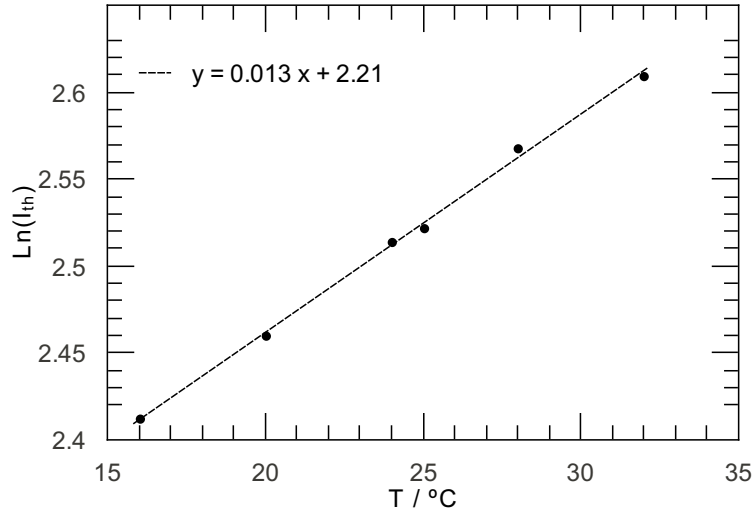


**Figure 3.3:** Figure showing the variations of the threshold current with the temperature.

increases, see table 3.1. A magnitude that measures the temperature sensitivity of the laser is the characteristic temperature  $T_0$  [22]. The threshold current varies with temperature corresponding to:

$$I_{th} \propto \exp\left(\frac{T}{T_0}\right), \quad (3.1)$$

Lower values of  $T_0$  imply that the threshold current increases more rapidly with temperature. Figure 3.3 depicts the variation of the threshold current with variations of temperature. The calculation of  $T_0$  for our laser gives us the following result:

$$T_0 = \frac{\Delta T}{\Delta \ln(I_{th})} = 79.37^\circ C,$$

T / °C	$I_{th}$ / mA
16	11.16
20	11.70
24	12.35
25	12.45
28	13.03
32	13.59

**Table 3.1:** Threshold current values as a function of the laser temperature.

*Variation of the Emission Wavelength with the Temperature*

Temperature also affects the emission wavelength of a laser diode. A drift in temperature of the gain medium shifts the wavelength of maximum gain and the cavity resonances. We measure experimentally this shift of wavelength with the optical spectrum analyzer (OSA). Figure 3.4 depicts the variation of the emission wavelength with the change in temperature for the two lasers we will use for synchronization experiments in chapter 5.

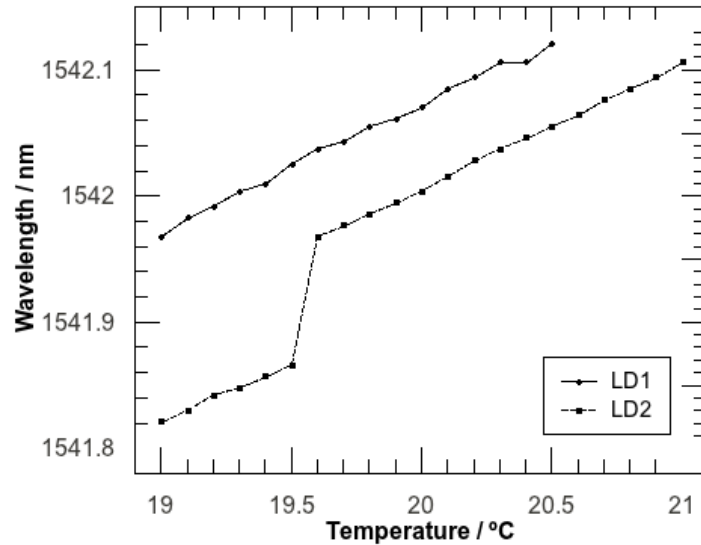


**Figure 3.4:** Variation of the emission wavelength with the changes in temperature.

We observe a linear variation of the emission wavelength with the variation of the temperature. Furthermore, both curves exhibit similar slopes. However, the curve of LD2 presents a sudden jump between 19.5 and 19.7 °C. This jump reflects a change in the longitudinal emission mode. The temperature drift modifies the maximum gain wavelength of the medium while the frequencies of the resonator modes do not shift to the same extent. This effect can cause, at certain temperatures, the power to switch to a competing mode with higher gain.

*Measurement of the Linewidth Enhancement Factor*

The linewidth enhancement factor ( $\alpha$ ) is a fundamental parameter for the dynamical behavior of a SL. This parameter represents the degree of broadening of the laser linewidth and is related to fluctuations in the carrier density that alter the refractive index and the gain medium. The linewidth is broadened by  $1 + \alpha^2$  [7] with respect to the linewidth predicted by Schawlow and Townes [5].

The linewidth enhancement factor can be measured in many different ways. Some methods use the change in emission wavelength and gain with carrier density. These

methods require a very precise knowledge of some laser parameters which are not always easily accessible. In this experiment, we have used the Henning-Collins method [23] to measure the linewidth enhancement factor. This method is based on measurements of the Fabry-Perot resonances in the spontaneous emission of the laser. The linewidth enhancement factor ( $\alpha$ ) is given by the following relation:

$$\alpha = \frac{2\pi}{\delta\lambda} \frac{d\lambda_i}{d\{\ln[(\sqrt{r_i} - 1)/(\sqrt{r_i} + 1)]\}}, \quad (3.2)$$

where  $\delta\lambda$  is the laser longitudinal mode spacing,  $\lambda_i$  is the  $i$ th mode wavelength and  $r_i$  is the ratio of the peaks to the trough in two consecutive longitudinal laser modes. The denominator represents the differential of an expression that is proportional to the net modal gain of each mode.

Figure 3.5 depicts the original spectrum from which we can extract the ratio of the peaks to the trough for the  $i$ th mode:

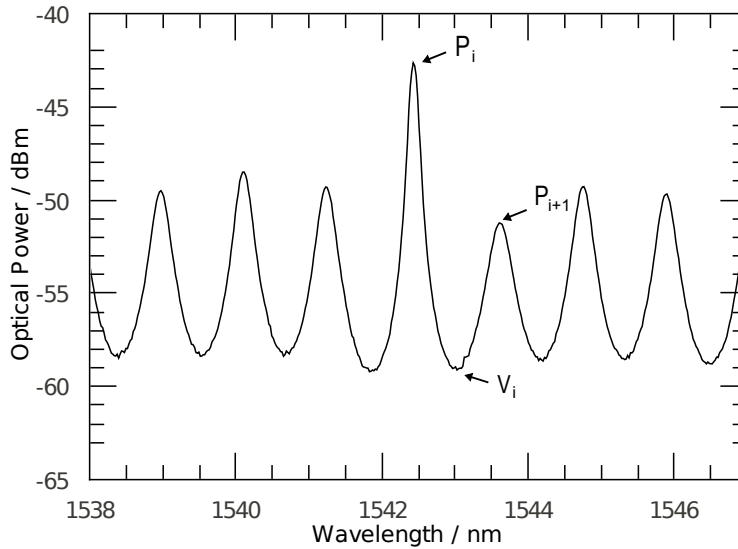


**Figure 3.5:** Scheme of the peaks-to-troughs ratio for the Henning-Collins measurement method.

We measure the slope of the wavelength shift versus the net modal gain for values of injection current under threshold. At each value of current, we measure  $r_i$  as follows:

$$r_i = \frac{P_i + P_{i+1}}{2V_i}, \quad (3.3)$$

The value of the linewidth enhancement factor for the laser used in the following experiments is  $\alpha = 1.76 \pm 0.02$ .

*Variation of the Relaxation Oscillations peak with the injection current*

The relaxation oscillation (RO) frequency reflects the fast time scales present in a SL and represents an upper modulation limit for SL devices. ROs are excited in the laser due to spontaneous emission or undamped by optical feedback. We can detect the characteristic frequency of the RO in the rf-spectrum of the ESA. Figure 3.6 depicts a power spectrum measured with the ESA for the DMLD in CW pumping at 1.06 times the threshold current. The RO peak can be observed around 1.3 GHz.

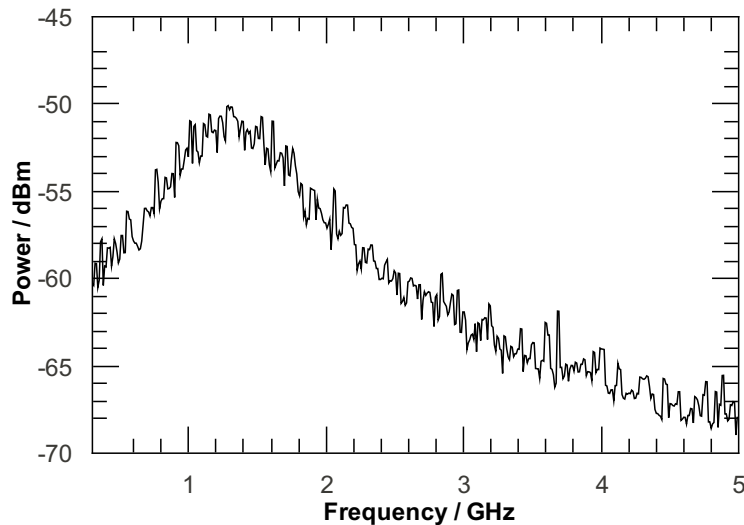


**Figure 3.6.** Experimental rf-spectrum of a DMLD. The laser is pumped  $I = 12.51$  mA ( $1.06 I_{th}$ ). The RO peak is around 1.3 GHz.

Figure 3.6 reveals a RO frequency peak for  $1.06 I_{th}$  around 1.3 GHz. As the injection current is increased, the RO peak shifts to higher frequencies. The characterization of this shift is important due to the role the RO play in the laser broadband dynamics. Furthermore, fast RO are desired for telecommunication applications. Relaxation oscillations up to several GHz play a key role for modern optical communications since such fast RO allow for direct modulation GBit/s telecommunication systems.

Figure 3.7 depicts the shift of the RO frequency peak with the injection current. This figure is obtained by changing the injection current and measuring the RO frequency peak. This measurement has some uncertainty that grows with the injection current due to the fact that the RO peak becomes less pronounced as the pump current increases. The error bars in figure 3.7 are related to this uncertainty and are measured as the frequency value at which the power in the rf-spectrum falls by 3 dB.

In section 1.3.1 we deduced from the rate equations formalism an expression for the characteristic frequency of the undamped ROs (equation 1.12). This relation

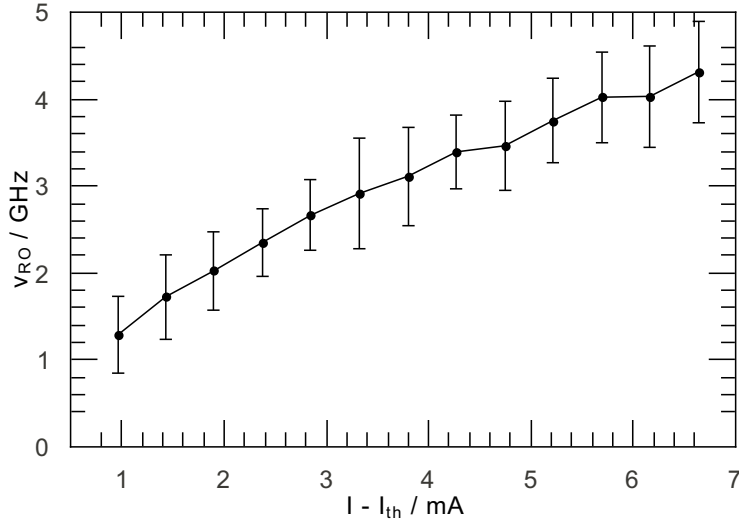


**Figure 3.7.** Dependence of the relaxation oscillation frequency on the pump current. The error bars correspond to the frequency values at which the power in the rf-spectrum falls 3 dB.

shows a proportionality between the RO frequency and the square root of the photon density inside the laser cavity. As we know from the explanation of the different slopes in the PI curve, a linear dependence exists between the injection current and the photon density for pump values sufficiently far above the threshold:

$$\omega_{RO} \propto \sqrt{N_p} \simeq \sqrt{I},$$

Our experimental measurement allows us to confirm the validity of this theoretical prediction. A log-log plot fits the experimental data with a slope corresponding to a power-law relation between both magnitudes. Figure 3.8 depicts the log-log plot of the data correspondent to figure 3.7. A linear fit of the data (dashed line) reveals a slope equal to 0.56.